Zn$_x$Ge$_{1−x}$O 3D Micronano Structures with Excellent Performance as Anode Material in Lithium Ion Battery

Y. Sun,[†,#] G. Z. Yang,[†,#] H. Cui,[‡,#] J. Wang,[§] and C. X. Wang*[,†,‡,#]

[†]State Key Laboratory of Optoelectronic Materials and Technologies, [‡]The Key Laboratory of Low-Carbon Chemistry & Energy Conservation of Guangdong Province, [#]School of Physics Science and Engineering, and [§]School of Chemistry and Chemical Engineering, Sun Yat-sen (Zhongshan) University, Guangzhou 510275, People's Republic of China

ⓢ *Supporting Information*

ABSTRACT: As anode material used in power storage device, lithium ion battery (LIB) for example, ZnO has not been recognized as a promising candidate, although which shows advantages like environmental benign, low cost, and large reservation. Several problems, such as volume expansion, pulverization, and active substance detachment because of the particular lithiation kinetics, which result in very high irreversible capacity and following fading, can account for the present situation. Here in this work, we report the self-assembly of Zn$_x$Ge$_{1−x}$O three-dimensional (3D) micronano structures and achieve enormous improvement on both recyclability and rate performance. After the 100th cycle, the capacity remains ∼690 mAh/g at the rate of 100 and ∼510

mA/g at the rate of 500 mAh/g. The capacity recovered rapidly even the rates alternating repeatedly between 50 mA/g and 3.5A/g. Ex situ observation reveals that substance detachment and nanoparticle agglomeration were avoided, benefiting from the firm 3D space configuration. As the Li$^+$ insertion, the 3D architectures fracture hierarchically with releasing the volume-expansion produced strain. Stable and smooth Li$^+$/electrons path would form in these nanoparticles integrated microfragments, which act as the working unit free of further detachment. These facts demonstrate that ZnO based anode materials are anticipant to be good candidate in LIB device through rational design of advanced mirco-nano structures without introduction of carbon coating.

KEYWORDS: self-assembly, three-dimensional nanostructures, Ge-doped ZnO, LIB, high capacity, long-term stability
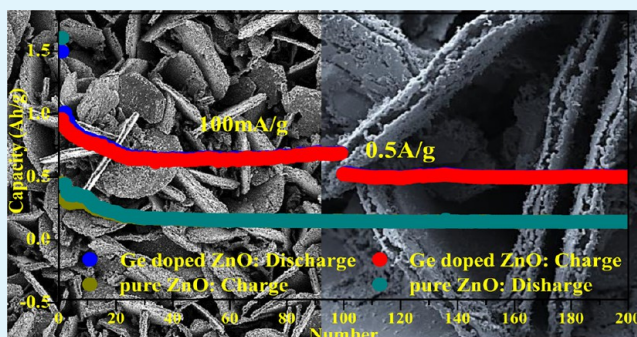
■ INTRODUCTION

For achieving advanced LIB anode electrode materials in low cost with long-term cyclability, high power capacity and fast rate capabilities, broad family of compounds ranging from simple substance (Si, Ge, Sn)[1−3] to binary oxide (SnO$_2$, Fe$_2$O$_3$, CoO, NiO, VOx)[4−8]/alloying materials[9,10] and ternary compound[11,12] have been investigated. Noticeably, there is very few impressive breakthroughs on ZnO anode materials by now, although which possesses many advantages such as low cost, large reserves and environmentally friendly.[13] With several problems like bad stability and rate performance, it seems hard to recognize ZnO as good candidate of LIB anode material[14,15] presently. Fortunately, benefiting from the advanced in situ TEM technology, scientists explored the structural and morphological evolution of crystal ZnO nanostructures during the alloying/dealloying reaction by vivid observation, which exposed the physical origin of the bad performance. For example, J. Li and his co-workers investigated the lithiated mechanism and structural evolution of ZnO nanowires, demonstrating in detail the leapfrog cracking and nano-amorphization, which results in the transformation of a single-crystal ZnO nanowire into a nanoglass with multiple glass nanodomains.[16] Su et al. found ZnO particles would crack

into fine nanoparticles during the first lithiation.[17] Eventually, the pulverization caused by volume change would further result in active substance detachment, as well as dramatically larger contact resistance due to the agglomeration of atomizing ZnO product when immersed in electrolyte, both of which would enhance the reversible capacity shrink. mechanism makes ZnO perform not very well on aspects of capacity and long-term cyclability when used as LIB anode material, although the theoretical capacity is as high as 978 mAh/g.[18,19]

In this case, two points must be proposed and solved simultaneously if ZnO could be used as high capacity and prolonged lifetimes anode materials: (1) rational design of nanostructures with more abundant electrochemical active sites and rich Li$^+$/electrons path; (2) prevent structure collapse, nanoparticle agglomeration and detachment resulted from atomizing effect during the discharge process. By now, Single-crystal ZnO nanostructure with various morphologies like nanowires and nanoparticles is easily achieved. However, item (2) cannot be solved effectively. The difficulty lies in the fact
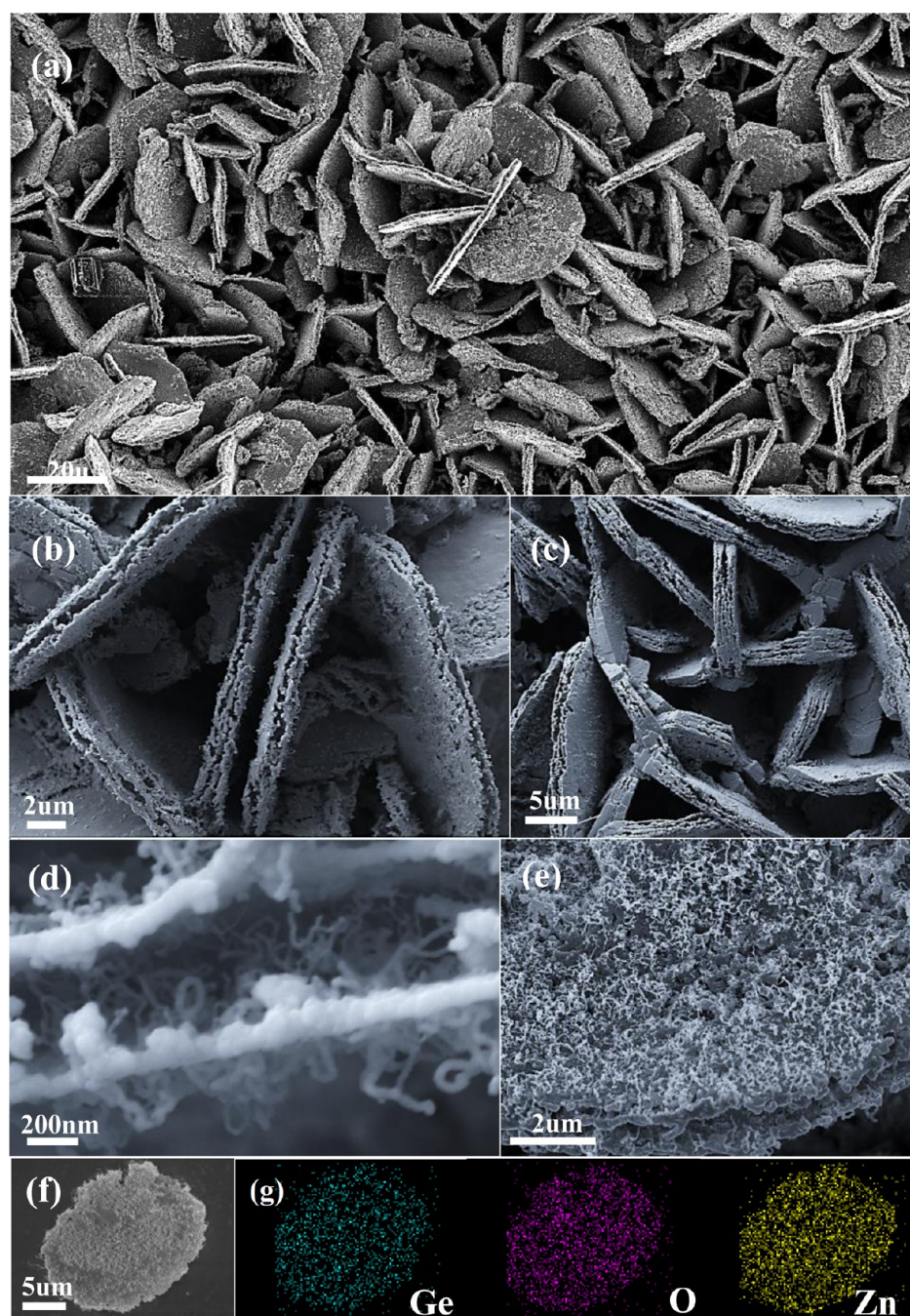
Figure 1. SEM characterization of the 3D micronano structures. (a) The typical low-magnification SEM image of the sample in large area. (b) Several units composed of double layers of nanosheet. (c) Higher magnification image of muti-layer 3D micronano structures. (d) The cross-section SEM characterization of a single structure. (e) The closer view on the surface of a nanosheet. (f) A single 3D micronano structure which was placed on Si substrate. (g) The EDS mapping analysis of the unit shown in panel f.

that there has no effective working mechanism for these pretty single-crystal structures to resist the negative influences above. The capacity would fade enormously during the first several cycles for both bulk ZnO and nanostructures. Recently, double-phase composite is recognized to be advantageous to overcome these problems. For example, nanoparticles of active materials being anchored on carbon skeleton (graphene, mesoporous carbon and amorphous carbon) are commonly considered.[20−25] Comparing to simple nanowires and nanoparticles, these configurations is useful to resist volume expansion, structure atomizing, collapse and then detachment due to the larger porosity and strong adhesion of the firm space structures. In

another way, if ZnO nanoparticles could be assembled in stable space dimensions, it may be also a good solution even without introduction of carbon.

Here in this work, we reported the self-assembly Ge doped ZnO ($Zn_xGe_{1-x}O$) 3D micronano structures composed of nanoparticles-constructed one-dimensional and two-dimensional (1D and 2D) nanostructures. We found that the 3D micronano structures perform well to improve the performance as LIB anode materials. After the 100th cycle, the capacity retains ~690 mAh/g at the rate of 100 mA/h and 510 mAh/g at 500 mAh/g. By investigating the morphological and structural evolution during the charge/discharge process with
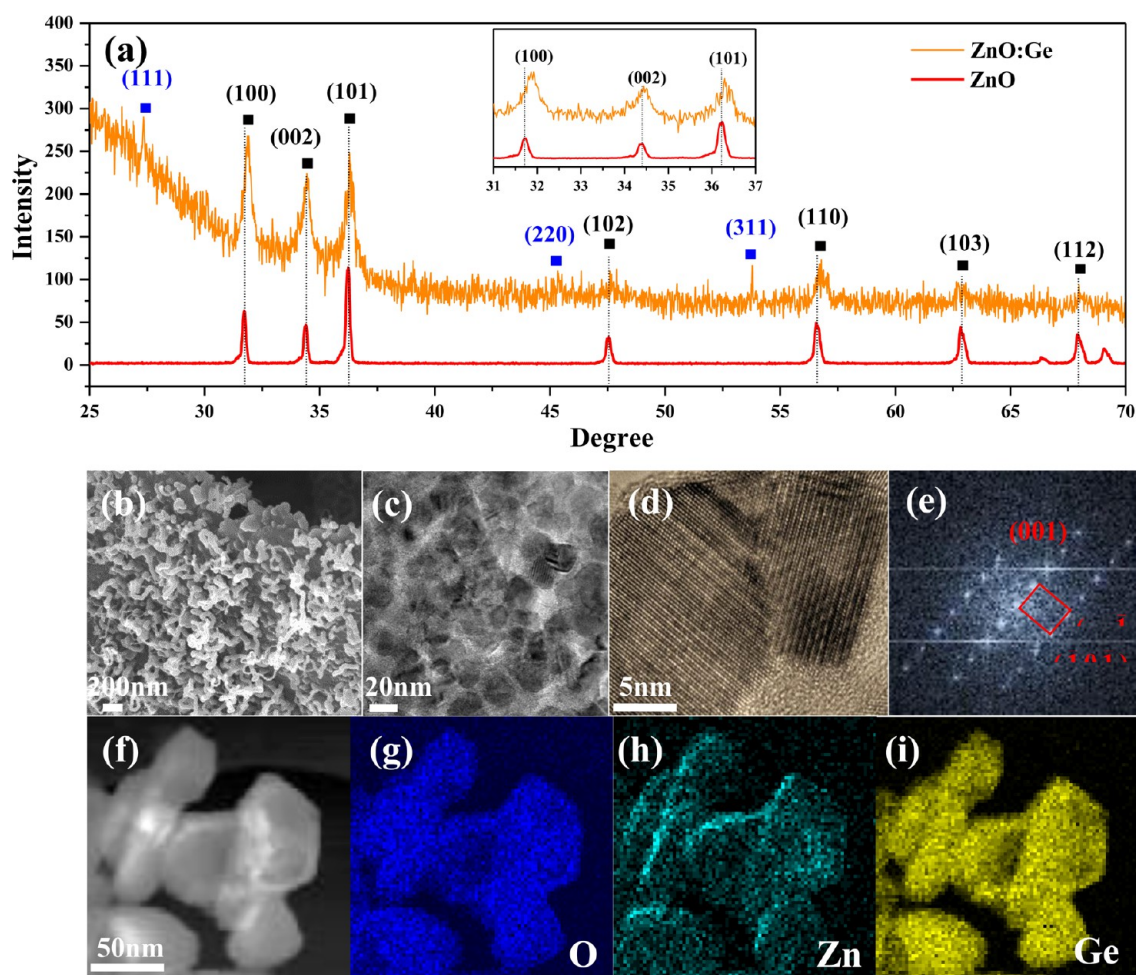
Figure 2. XRD and TEM analysis of the sample. (a) The XRD pattern of the product, the inset is the closer inspection of the pattern ranging from 31 to 37°. (b) High magnification SEM image of the surface of the 3D micronano structure. (c) The typical bright field TEM image of the sample. (d) The HRTEM analysis of several nanoparticles. (e) The FFT pattern corresponding to the marked area in panel d. (f) STEM image of several particles with large size at the edge area. (g–i) TEM EDS mapping of the particles, corresponding to O, Zn, and Ge, respectively.

ex situ method, we found the novel configuration experienced a hierarchically fracture process, which results in a buffering mechanism upon excessive stress because of volume expansion. In detail, there are several features that account for the improved performance: (1) with nanoparticles as fundamental of the architecture, the 3D micronano structures have rich electrochemical active sites due to the large surface area; (2) the firm space architecture of the novel 3D configuration can resist both active substance detachment and agglomeration during repeated cycling although atomizing effect occurred; (3) porous and multichannel features result in a smooth transport of electrons/Li$^+$, and Ge dopant would also enhance the electron conductivity.

■ EXPERIMENTAL SECTION

The 3D Zn$_x$Ge$_{1-x}$O micronano structures were prepared in chemical vapor deposition (CVD) system, which was illustrated in previous works.[26−28] In detail, mixture of ZnO and C black (30 mg, atomic ratio 2:1) was put at the center of a polished ceramic sheet and GeO$_2$ powder (5 mg) was placed by side. The whole ceramic sheet is pushed into a semiclosed corundum tube, which is pushed into the furnace with ZnO/C powder at the central position of the heating elements. After being pumped by a mechanic pump, the chamber vacuum degree reached as high as ∼10^{-1} Pa. H$_2$ at a flow of 100 sccm and CH$_4$ at a flow of 5 sccm was introduced until the pressure of the chamber

reached 20 kPa. At the same time, the temperature was raised to 1150 °C step by step in 50 min. Both of the pressure and temperature was hold for 120 min. After the process, brown product in large area which was independent of substrate could be found at low temperature zone.

Electrochemical tests were carried out in a two-electrode electrochemical cell by using lithium foil as a counter-electrode and the sample as working electrodes. The working electrodes were prepared by mixing the active material, carbon black, and polyvinylidene fluoride (PVDF) in a weight ratio of 7:2:1 in N-methylpyrrolidinone (NMP), which was coated uniformly on copper foil by an automatic thick film coater (AFA-I). The weight of the active substance is 0.26−0.33 mg/cm^2. After drying in a vacuum chamber at 120 °C for 12 h, the foil was rammed by an electromotive roller (MR-100A) and tailored to the appropriate size by a coin-type cell microtome (T-06). The final cell was fabricated using a polypropylene micromembrane as the separator (Celgard, 2400, USA); 1 M LiPF6 in ethylene carbonate (EC) and diethyl carbonate (DEC) with a weight ratio of 1:1 served as the electrolyte. Cyclic voltammetry of the cell was scanned at 0.1 mV/s in the voltage range of 0.001−2.5 V (versus Li/Li+) on an Ivium electrochemical workstation. The discharge−charge measurement of the cells was carried out at room temperature using a multichannel battery tester (Shenzhen Newware Technology Limited Co., China).

■ RESULTS AND DISCUSSION

Figure 1 is the SEM images of the sample in various magnifications, from which a lot of nanoplates with rough
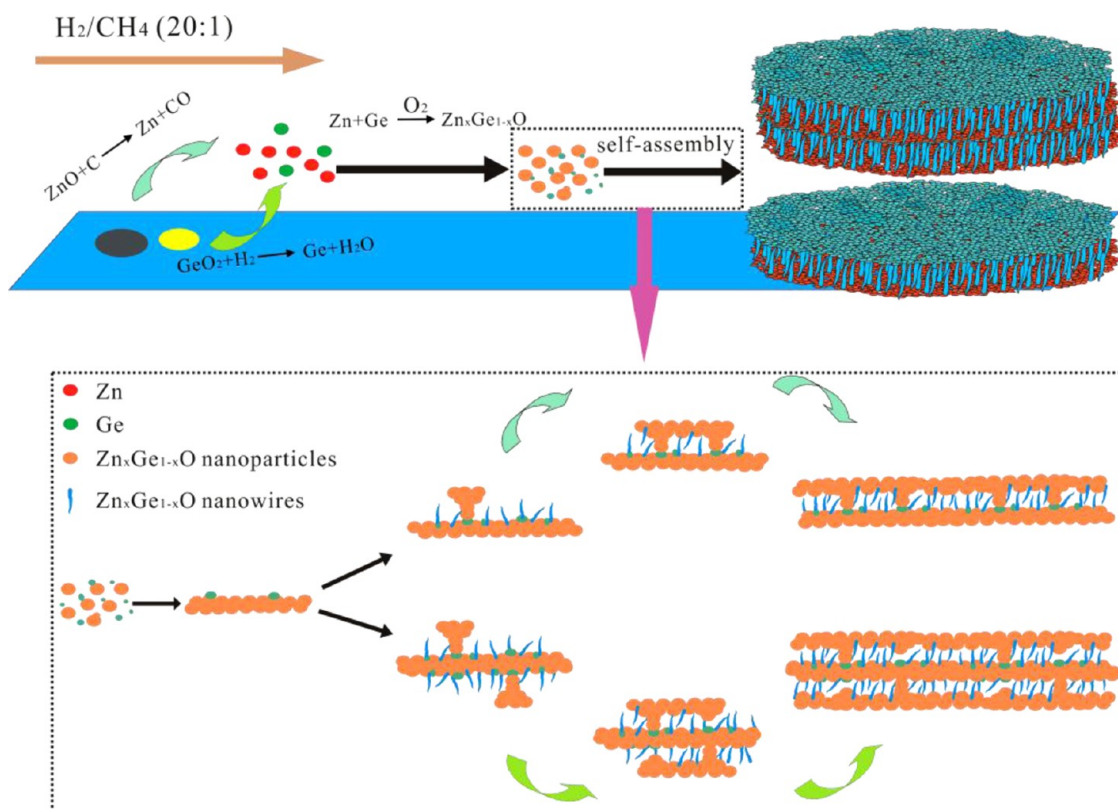
Figure 3. Self-assembly illustration of the Zn_xGeO_{1-x} 3D micronano structures.

surfaces are exhibited. Noticeably, as shown in panels b and c, the micronano units are actually self-assembled novel 3D structures constructed layer by layer with smaller 1D and 2D nanostructures. Figure 1c exhibits several 3D micronano structures constructed by muti-layer nanosheets. The 3D units with different layers have the same self-assembly mechanism that would be demonstrated below. Figure 1d is the closer view of a single unit, which is composed of two layers of nanoplates anchored by irregular 1D nanostructure. These short nanowires grow from the lateral surface with diameter less than 20 nm (similar to the sizes of nanoparticles). Figure 1e shows a lateral surface of a single unit, on which we can see clearly the rough surface and short nanowires. To confirm its elemental information, a single one was placed on a silicon substrate and investigated with energy diffraction spectrum (EDS) mapping, as shown in Figure 1f. Like Zn and O, there is a uniform distribution of Ge element. Noticeably, EDS mapping carried out under TEM, which has a higher resolution, further confirms the Ge dopant distribution, as shown in Figure 1g.

Figure 2a exhibits the XRD pattern of the sample, in which ZnO (PDF #36-1451) and tiny Ge (PDF #04-0545) are detected. All of the diffraction peaks are marked with plane index as shown. Noticeably, several peaks display some shift comparing with phase-pure ZnO. The closer view shown as inset indicates that the peaks have different shift to standard pattern. This exclude the possibility that the shift is common error resulted from regular test, which implies the product may be decided to be Ge doped ZnO. both of ionic Ge^{2+} (73 pm) and Ge^{4+} (53 pm) have a smaller radius than Zn^{2+} (74 pm), it is reasonable that Ge doped ZnO has a smaller space distance than pure ZnO. Figure 2b is a typical SEM image corresponding to a piece of Ge doped ZnO sheet, and Figure 2c is the TEM image, from which clear particles with sizes less than 20 nm can be seen. The HRTEM analysis and corresponding FFT (Fast Fourier transform) pattern shown in Figure 2d–e further indicates the ZnO lattice. We chose several particles with size as large as 50 nm to employ nanodomain elemental analysis as shown in panels f–i. According to the EDS mapping, Ge element exists in the ZnO particle and displays a full distribution. However, it implies there is Ge enrichment at local edge area. The nanowires on the nanosheet are also characterized using HRTEM, as shown in Supporting Information Figure S1. The diameter of a polycrystalline nanowire is similar to the size of a particle. Actually, there is also no obvious difference of the composition between them based on EDS analysis, which is not provided here.
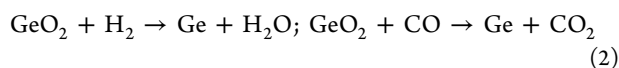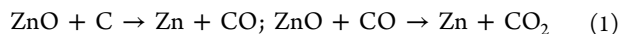
As well-known, XPS is a very powerful tool to employ chemical state analysis. Here, it was used to characterize the Ge element. The result was presented as Supporting Information Figure S2, which decides the binding energy of Ge at 31.48 and 29.55 eV. The latter one points to pure Ge,[29] while the former signal is from Ge–O bond, which shifts lower than in GeO_2 (32.5–33.1 eV).[30] We believe the peak can be finally attributed to the Ge atoms occupying Zn sites in ZnO lattice, which is consistent to the analysis from XRD pattern. Here, we analyzed the data quantitatively and decided the Zn/Ge ratio is about 5.9. At the same time, the atomic ratio between Ge–O and Ge–Ge is determined to be 6.5, which is to say that the value of x in $Zn_xGe_{1-x}O$ is approximately 0.86. On the other hand, the UV spectrum of the sample displays obvious difference to pure ZnO powder with the main absorption peak shift to blue direction as shown in Supporting Information Figure S3. Additionally, comparing to the pure ZnO, the UV absorption of Ge doped ZnO nanoplates displays a platform ranging from 400
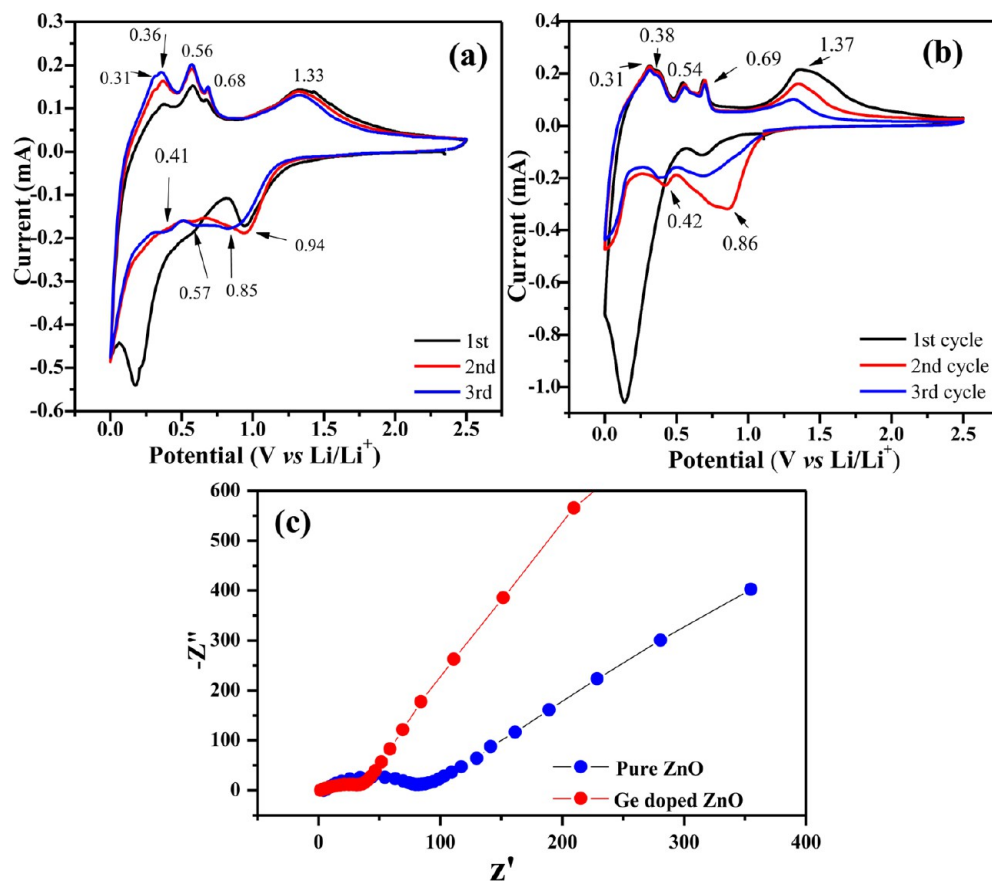
Figure 4. Electrochemistry cyclic voltammograms (CVs) measurement and impedance analysis of the cell using Zn_xGeO_{1-x} 3D micronano structures as anode material, with comparing to pure ZnO material. (a) The CV curves of Zn_xGeO_{1-x} corresponding to the first three cycles. (b) The CV curves of pure ZnO, (c) The measured impedance after the discharging process.

to 550 nm. The signal may be from the additional levels related to Ge doping, which is similar to other cases of doped ZnO.[31,32]

The self-assembly of 3D $Zn_xGe_{1-x}O$ micronano structures is a very interesting process that could be demonstrated by a liquid-Ge assisted VS (vapor−solid) priory physicochemical mechanism. It is critical that GeO_2 powder and ZnO/C mixture were chosen as precursor, both of which are liable to be transported synchronously above 1000 °C. Except for helping to reduce ZnO to Zn, CH_4-derived carbon play an important part to resist the agglomeration of Zn clusters during the transport, because which provides absorption sites for small Zn clusters. H_2 acted as carrier gas as well as gaseous reductant. The growth and self-assembly mechanism can be illustrated as Figure 3. At target temperature, the following reactions would occur

$$ZnO + C \rightarrow Zn + CO; \quad ZnO + CO \rightarrow Zn + CO_2 \quad (1)$$

$$GeO_2 + H_2 \rightarrow Ge + H_2O; \quad GeO_2 + CO \rightarrow Ge + CO_2 \quad (2)$$

As soon as being reduced and then vaporized, Ge and Zn clusters would transport independently without combination according to the binary phase diagram. Noticeably, there is a O-rich region during the transport of source materials, although the reaction occurs in reducing environment. After Ge and Zn combing with active oxygen in O-rich zone during transportation that is usually in low temperature zone, liquid GeO_2 and solid ZnO nanoclusters would be attached to each other physically and then alloying, forming $Zn_xGe_{1-x}O$. The initial

step of the self-assembly is to form $Zn_xGe_{1-x}O$ quasi-2D nanostructures, in which ZnO is host phase with Ge as dopant. By now, the growth of 2D polycrystalline nanosheet mainly dominated by VS mechanism is very common, which has been investigated a lot with experimental and theoretical methods.[33−35] Herein, we would not like to demonstrate this process in detail, the main focus would be on the assembly of 3D micronano structures. Actually, Ge clusters in liquid form play an important part in this procedure as shown in Figure 3. In this process, residual liquid Ge would adhere to $Zn_xGe_{1-x}O$ nanoparticles, serving as binder by welding the adjacent particles. Noticeably, the size of Ge binder is very small and not ubiquitous so that we did not observe clear Ge signal by EDS mapping and HRTEM easily. The active Ge clusters on the nanosheet surfaces would enhance the deposition of $Zn_xGe_{1-x}O$ phase due to absorption effect on the solide-liquid interface. In this circumstance, spikes perpendicular to $Zn_xGe_{1-x}O$ nanosheet would grow out as shown in the Figure 3, which provides a nucleating point in another space plan parallel to the existing nanosheet. Another nanosheet would finally form side by side. The two parallel 2D structures are stapled together by the spikes, which build a firm 3D architecture. The trilaminar and four-storeyed units share the same mechanism. On the other hand, there are Ge-rich regions on the rough surfaces of the polycrystalline nanosheet that are convenient to nucleate for $Zn_xGe_{1-x}O$, which demonstrates the origin of vertical nanowires distributing on inner and outer surface of the 3D micronano structures. Noticeably, as the fundamental building block, most of the nanoparticles own the
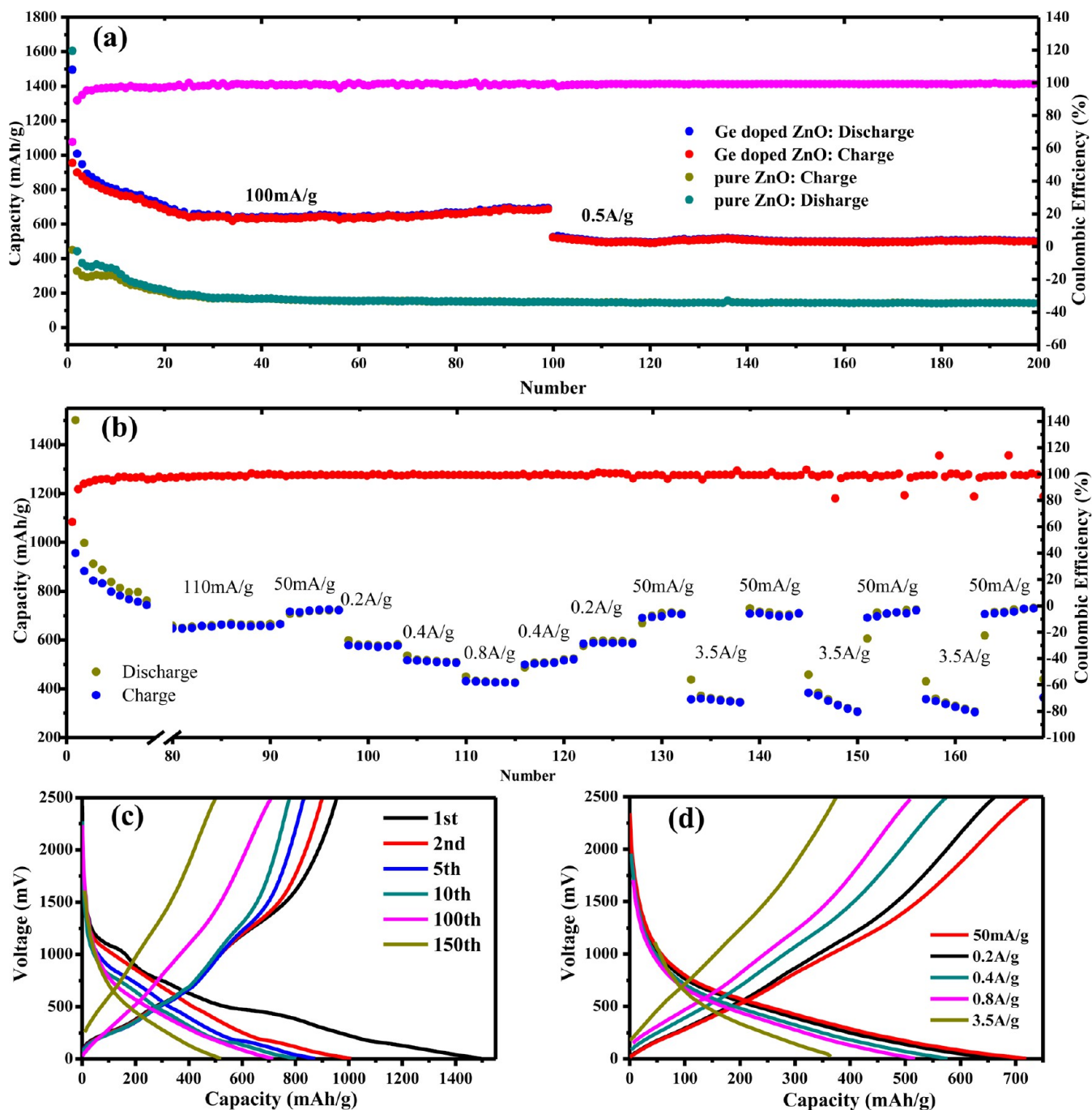
Figure 5. LIB cyclic stability test and rate performance of the sample. (a) Cyclic stability test at the rate of 100 mA/g for 100 cycles and another 100 cycles at the rate of 0.5A/g followed, in which phase-pure ZnO powder was used as reference. (b) Rate performance of the cell. (c) The specific capacity−voltage curves corresponding to 1st, 2nd, 5th, 10th, 100th, and 150th cycles. (d) The specific capacity−voltage curves at various rates.

similar size less than 20 nm. It is probable that the nanoparticles nucleated simultaneously with diverse crystal orientation in a very short time range, which resulted in smaller particle sizes. Yu et al. have done much research on the nanostructure self-assembly of metal carbonate and sulfate. Different environment condition and crystallized time would cause a self-limited effect, which plays a very important part to the following growth of 3D structures.[36−38] We think there is something common in our case.

The 3D $Zn_xGe_{1−x}O$ micronano structures were assembled in a half-cell with lithium as counter electrode. Cyclic voltammo-grams (CVs) of the sample was tested between 0.005 and 2.5 V

at a scan rate of 0.2 mV/S, which is presented as Figure 4a. In the previous study, many works have confirmed that ZnLi is the intermediate of ZnO after being reduced, which has been supported by CV and HRTEM.[14,17] When applied as anode materials storing Li^+, GeO_2 would be reduced to Ge and then alloys with Li. The second reaction is reversible and produce repeated charge/discharge capacity.[39−41] According to these results, we analyzed obtained CV curve as below. In the first cathodic process, there is a intense peak at 0.94 V attributed to the reduction of ZnO into Zn, while the weak peak at about 0.57 V may be from the influence of tiny Ge phase which is absent in the CV curve of phase-pure ZnO as shown in Figure
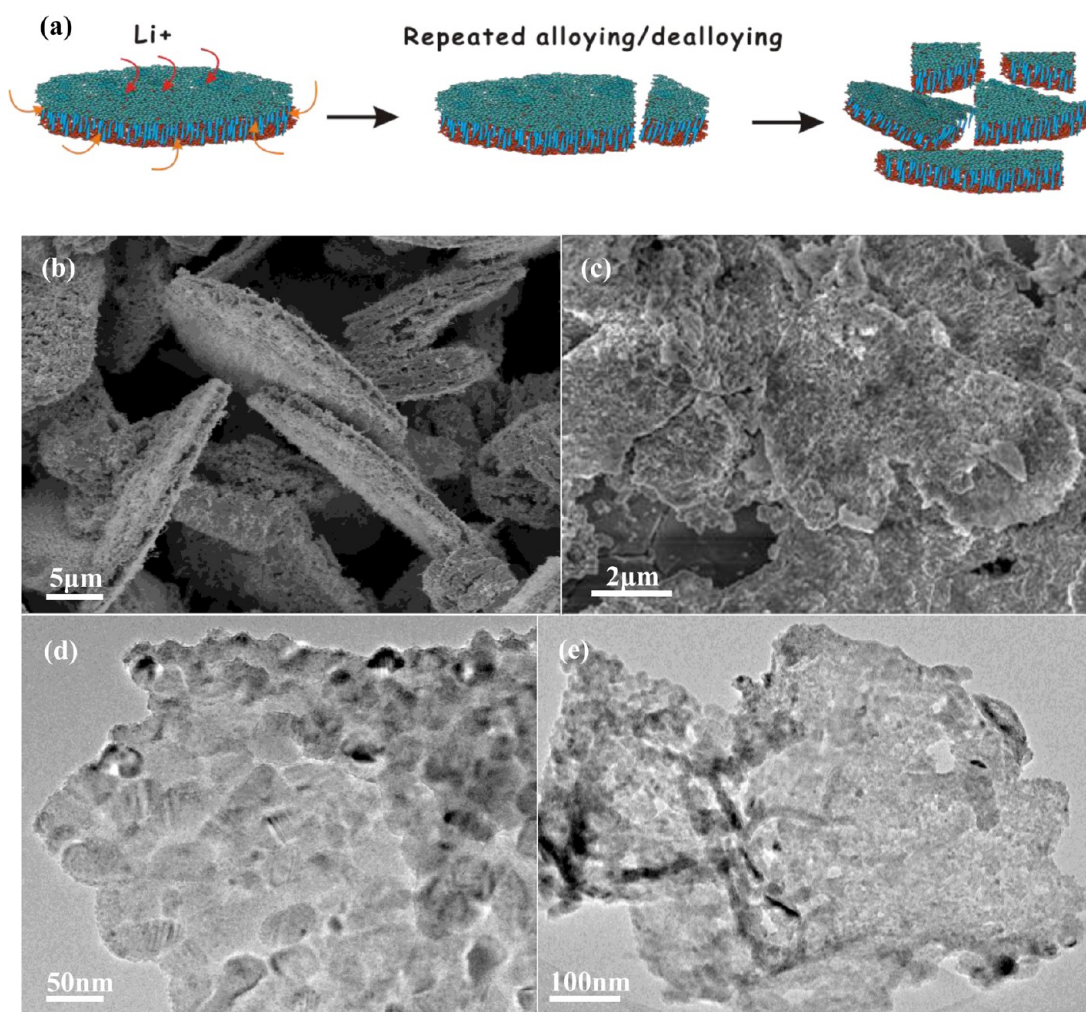
Figure 6. Morphology evolution of the Zn_xGeO_{1-x} 3D micronano structures against the repeated alloying/dealloying process. (a) Illustration diagram of the morphological variation of the micronano structure. (b) SEM image of the Zn_xGeO_{1-x} 3D micronano structures before lithiation. (c) SEM image after repeated cycles. (d) TEM characterization of the initial Zn_xGeO_{1-x} 3D micronano structures. (e) TEM image of a piece of the fragment after repeated cycles.

4b. The broad signal ranging from this peak to 0.17 V imply complex reaction process including the decomposition of electrolyte and the Zn−Li alloying reaction.[14,42] In the second and third cathodic procesps, the signal at 0.17 V almost disappears and other several peaks at 0.94 and ∼0.41 V are distinguished, which expose the reversible feature of ZnO−Zn and Zn−ZnLi transformation, respectively. Additionally, the signal at 0.57 V corresponding to Ge−Li reaction is also visible, which indicates that the Ge dopant contributes to the reversible capacity. In the anodic scan, there are four obvious peaks ranging from 0.2−0.7 V detected, which locate at 0.31, 0.36, 0.56, and 0.68 V, respectively. As reported earlier, these redox processes correspond to the multistep delithiation process of ZnLi, that is, $LiZn \rightarrow Li_2Zn_3 \rightarrow LiZn_2 \rightarrow Li_2Zn_5 \rightarrow Zn$.[43] The following peak at 1.35 V implies the decomposition of Li_2O.[42] Noticeably, we cannot match the oxidation peak of $GeLi_x$ (0.5−0.7 V) here because the signal is so weak that it has been covered by other peaks attributed to the oxidation of Zn. On the other hand, the CV curve of phase-pure ZnO exhibits an obvious reversible capacity loss during the repeated cycles. Moreover, electrochemical impedance related to both of the samples as an anode electrode was tested as shown in Figure 4c. they were collected under the same condition such as the cell

assembly technology, scanning speed and so on. Accordingly, it can be concluded that the introduction of Ge element in ZnO lattice help to decrease the cell resistance enormously. On the other hand, the CV measurement clarifies that the complete electrochemical process includes the redox between Ge−O and Ge−Li, which is similar to the work reported by Bresser et al.[44] They investigate transition-metal-doped ZnO nanoparticles as a lithium-ion anode material.

Figure 5 shows galvanostatic cycling performance of 3D $Zn_xGe_{1-x}O$ micronano structures, which was collected at a rate of 100 and 500 mA/g between 0.005 and 2.5 V in coin type half cell. Device made of phase-pure ZnO using the same technology was investigated as a reference. The capacity of pure ZnO drop to ∼460 mAh/g after the second discharge at the rate of 100 mAh/g, although the capacity corresponding to the first discharge is as high as 1600 mAh/g. During the following cycles, the capacity decreased to ∼150 mAh/g gradually. The observed irreversible capacity in the first cycle is mostly due to the formation of solid electrolyte interface (SEI) layer which increased internal resistance and caused larger impedance of Li ion transport. The rapid capacity decrease during the consecutive cycles originates from the particle pulverization due to large volume expansion during alloying/

Table 1. Comparison of the Lithium Storage Performance of ZnO-Based Anode Materials

	ZnO-based anode materials	lithium storage performance		
		current density	cycle number	discharge capacity (mAh/g)
carbon coating and skeleton	yolk-shell ZnO−C microspheres[39]	100 mA/g	150	520
	flower-like ZnO−NiO−C films[40]	1 C	50	380
	Zn−Al$_2$O$_3$−C nanocomposite[41]	100 mA/g	100	400
	ZnO quantum dot/graphene nanocomposites by ALD[42]	100 mA/g	100	540
	carbon-coated Zn$_{0.9}$Fe$_{0.1}$O nanoparticles[43]	48 mA/g	30	800
present work	**Zn$_x$Ge$_{1−x}$O 3D micronano structures**	**100 mA/g**	**100**	**690**
		500 mA/g	**>100**	**510**
free of carbon	ZnO nanorods[14]	0.1 mA/cm^{-1}	40	310
	porous ZnO nanosheets[37]	500 mA/g	100	400
	hierarchical flower-like ZnO nanostructures−Au nanoparticles[36]	120 mA/g	50	382
	Al$_2$O$_3$-doped ZnO films[18]	2 μA cm^{-2}	40	590
	SnO$_2$/ZnO composite[44]	120 mA/g	40	497

dealloying process. Obvious pulverization would leads to continuous loss of active material, which can accounts for the capacity decrease. These features imply that pure ZnO is hard to be applied as LIB anode materials.

However, self-assembled 3D Zn$_x$Ge$_{1−x}$O micronano structures displayed an impressed performance, which had a higher reversible capacity. The first charge and discharge capacity were 1496.5 mAh/g and 1014 mAh/g respectively, delivering a Coulombic efficiency of 67.8%. Although the anode exhibited a decreased capacity generally during the first 20 cycles in the long term cyclic stability test, it finally provided a stable capacity of ∼690 mAh/g at the rate of 100 mA/g. When the charge/discharge rate changed to be 0.5A/g after the 100th cycle, the device still runs well with the capacity of ∼510 mAh/g.

Furthermore, we examined the rate performance of the anode materials, as shown in Figure 5b. After the 90th cycle at the rate of 110 mA/g, the anode was tested with the cycling rates of 50, 200, 400, and 800 mA/g, at which the recorded capacity was ∼720, ∼570, ∼515, and ∼430 mAh/g, respectively. The Coulombic efficiency remains above 90% during the whole process, demonstrating an excellent cycling stability at higher charge/discharge rates even after long period cycling. To examine the performance when the device was switched between low and high charge/discharge rates, the anode was tested at rates of 50 mA/g and 3.5A/g alternatively without any other break, as shown in Figure 5b (after 132th cycle). The anode delivers a capacity of 360 mAh/g at the rate of 3.5A/g, which is similar to the theoretical capacity of graphite. Strikingly, while the rate returns to 50 mA/g, the capacity recovers to ∼700 mAh/g rapidly and the cell performs well with repeated alternation. Figure 5c and d are voltage profiles of Ge-doped ZnO sample corresponding to cycling stability test and rates performance. The curves exhibit good coherence with CV measurement. Above test indicates that the novel structures displays obvious advantages to phase-pure ZnO powder, which can be attributed to the better Li ions/electrons transport through the self-assembled nanostructures and the ability to resist pulverization collapse because of the solid three-dimensional architectures. Although the original unit would divide into several pieces as a result of large area and local stress produced as shown in Figure 6c, smooth Li$^+$/electrons path has been established. Furthermore, we made a comparison of the performance between various ZnO-based anode materials, including ZnO−C hybrids and pure ZnO phases, as shown in Table 1. The present Zn$_x$Ge$_{1−x}$O 3D

micronanostructures delivers a better capability and rate performance even comparing to the ZnO−C composites. The following analysis with ex situ SEM and TEM methods demonstrate these points well.

For pure ZnO anode material, the unwanted influence, like low-Coulombic efficiency and capacity fading, is most serious during the first several cycles. A single nanoparticle is ready to break into fine powder when ZnLi forms, which has been investigated carefully by Su. et al.[17] in the following cycles, these newly formed powder would easy to fall off. The large irreversible capacity exactly originates from the active material detachment resulted from the volume expansion and pulverization. Here, the designed Zn$_x$Ge$_{1−x}$O nanoparticles based 3D micronano structures provide stress-buffering mechanism hierarchically, which help to avoid these disadvantages and improves the performance enormously. As shown in Figure 5, the first Coulombic efficiency of Zn$_x$Ge$_{1−x}$O is as high as 66.7%, while the value of phase-pure ZnO is 27.3%. Here, phase-pure ZnO powder as anode material was investigated with simple SEM method, in order to observe its morphology evolution with the Li$^+$ insertion/extraction process as shown in Supporting Information Figure S4. Supporting Information Figure S4a is the morphology of ZnO microcrystals, most of which have regular hexagon prism shape. After the first discharge process, volume expansion and active substance detachment occurs, as in panel b. Figure S4(c), Supporting Information, display the typical morphology of the anode after 100th cycle, in which obvious pulverization effect is presented. These analyses can explain the origin why pure ZnO is hard to be applied as LIB anode materials.

There are several reasons that can account for the improved performance of Ge doped ZnO. First, the theoretical capacity of Zn$_{0.86}$Ge$_{0.14}$O is calculated to be ∼1030 mAh/g, which is higher than the value 980 mAh/g of phase-pure ZnO. Second, the Ge dopant enhances the electron conductivity, as the impedance analysis shown in Figure 4 (c), thereby improve the rate performance. Actually, the novel configuration is advantageous to help to resist the agglomeration after the nanostructures being pulverized. Figure 6 exhibits the morphology evolution of the anode materials along with the repeated lithiation/delithiation process. The sketch model shown as Figure 6a illustrate that the 3D micronano structures broke into several pieces accompanying with the lithiation process. The cracks often occurred along the route that is faint to resist local stress due to lithiation expansion, that is, thinner region and large particles rich area. Repeated cyclic process finally forces the

initial 3D micronano structures to be broken hierarchically in order to digest the produced stress in the whole unite, until the formed configuration could provide a stable lithiation/delithiation path free of excessive local stress. Figure 6c is the image of the anode material after the repeated cycles, which broke into several parts as a result of the volume expansion. Figure 6d and e correspond to the TEM images of the initial Ge doped ZnO nanofragment and the counterpart after repeated lithiation/delithiation process. According to these images, although the ZnO nanoparticles experienced a pulverization after cycles by forming thinner particles, the 2D configuration remain integrated without obvious nanoparticles agglomeration and detachment, which avoid the adverse influence like larger resistant and reduced Li$^+$ paths. Therefore, it is common that the capacity displays a slow increase in the long term test, as shown in Figure 5a. Eventually, the broken chip would result in much more electrochemistry active sites and shorten the Li$^+$ transport length. Moreover, the shape would be further maintained because they have experienced repeated charge/discharge process, which have release much stress and built reasonable space-path for Li$^+$/electrons exchange.

HRTEM was applied to observe the particle size variation during the first discharge. Figure 4 exhibits the TEM analysis of the anode material after discharging to be 0.25 V. Figure S5a and b, Supporting Information, corresponds to the images of a piece of fragment in low magnification, in which particles cannot be distinguished clearly on the scale bar of 20 nm. Figure S5(c), Supporting Information, is the SAED pattern of the marked area. Supporting Information Figure S5d is the image in higher magnification. The size of observed nanoparticles decreased to be about 5 nm as marked in the figure, while it is about 20 nm before discharge. HRTEM analysis indicates that these smaller particles correspond to Zn and ZnLi. Supporting Information Figure S6 is the HRTEM analysis when the cell discharges to 0.005 V. Figure S6a, Supporting Information, is the low magnification image, and Supporting Information Figure S6b is the SAED pattern, which was decided to be polycrystalline diffraction rings of Zn and ZnLi as marked. Supporting Information Figure S6c shows the HRTEM image corresponding to the edge of a piece of fragment, in which the phase and interplanar spacing were marked using red (ZnLi) and blue (Zn) typeface. As one can see, the size of the particles decreased further to be less than 5 nm. These facts demonstrate that the pulverization progress a lot during the first discharge. Noticeably, the fine particles maybe include GeLix in amorphous form. Supporting Information Figure S7 is the TEM analysis of the anode material after being charged again to 2.5 V. As mostly reported, ZnO finally formed after the dealloying process. Surprisingly, even after 100th cycle, the broken fragments still maintain the 2D structures without obvious active material detachment, as shown in Figure S8, Supporting Information.

CONCLUSION

In summary, $Zn_xGe_{1-x}O$ 3D micronano structures were achieved with one-step self-assembly method in CVD system. Ge played an important role in the growth process, serving as dopant and binder for the nanoparticles. The novel configuration delivered excellent LIB performance as anode material with capacity of ∼680 mAh/g at the rate of 100 mA/g. Moreover, the capacity was ready to recover even the rate switching between 50 mA/g and 3.5A/g. the enhanced capacity, stability and rate performance originated from the advantages

of the material, such as firm 3D configuration, free of detachment and strain-release mechanism. Stable and smooth Li$^+$/electrons transport path could form finally in the broken $Zn_xGe_{1-x}O$ fragments.

ASSOCIATED CONTENT

Ⓢ Supporting Information

UV absorption spectrum, XPS results, and HRTEM characterization of the sample after discharging. The Supporting Information is available free of charge on the ACS Publications website at DOI: 10.1021/acsami.5b02518.

AUTHOR INFORMATION

Corresponding Author

*Tel./Fax: +86-20-84113901. E-mail: wchengx@mail.sysu.edu.cn.

Notes

The authors declare no competing financial interest.

ACKNOWLEDGMENTS

REFERENCES

(1) Gu, M.; Yang, H.; Perea, D. E.; Zhang, J. G.; Zhang, S. L.; Wang, C. M. Bending-Induced Symmetry Breaking of Lithiation in Germanium Nanowires. *Nano Lett.* **2014**, 14, 4622−4627.

(2) Huang, X. K.; Yang, J.; Mao, S.; Chang, J. B.; Hallac, P. B.; Fell, C. R.; Metz, B.; Jiang, J. W.; Hurley, P. T.; Chen, J. H. Controllable Synthesis of Hollow Si Anode for Long-Cycle-Life Lithium-Ion Batteries. *Adv. Mater.* **2014**, 26, 4326−4332.

(3) Li, N.; Song, H. W.; Cui, H.; Wang, C. X. Sn@Graphene Grown on Vertically Aligned Graphene for High-Capacity, High-rate, and Long-life Lithium Storage. *Nano Energy* **2014**, 3, 102−112.

(4) Zhu, J.; Zhang, G. H.; Yu, X. Z.; Li, Q. H.; Lu, B. A.; Xu, Z. Graphene Double Protection Strategy to Improve the SnO2 Electrode Performance Anodes for Lithium-ion Batteries. *Nano Energy* **2014**, 3, 80−87.

(5) Yang, Y.; Fan, X. J.; Casillas, G.; Peng, Z. W.; Ruan, G. D.; Wang, G.; Yacaman, M. J.; Tour, J. M. Three-Dimensional Nanoporous Fe$_2$O$_3$/Fe$_3$C-Graphene Heterogeneous Thin Films for Lithium-Ion Batteries. *ACS Nano* **2014**, 8, 3939−3946.

(6) Liu, J. C.; Xu, Y. J.; Ma, X. J.; Feng, J. K.; Qian, Y. T.; Xiong, S. L. Multifunctional CoO@C Metasequoia Arrays for Enhanced Lithium Storage. *Nano Energy* **2014**, 7, 52−62.

(7) Chen, X. Y.; Zhu, H. L.; Chen, Y. C.; Shang, Y. Y.; Cao, A. Y.; Hu, L. B.; Rubloff, G. W. MWCNT/V$_2$O$_5$ Core/Shell Sponge for High Areal Capacity and Power Density Li-Ion Cathodes. *ACS Nano* **2012**, 6, 7948−7955.

(8) Zhou, G. M.; Wang, D. W.; Yin, L. C.; Li, N.; Li, F.; Cheng, H. M. Oxygen Bridges between NiO Nanosheets and Graphene for Improvement of Lithium Storage. *ACS Nano* **2012**, 6, 3214−3223.

(9) McDowell, M. T.; Lee, S. W.; Nix, W. D.; Cui, Y. 25th Anniversary Article: Understanding the Lithiation of Silicon and Other Alloying Anodes for Lithium-Ion Batteries. *Adv. Mater.* **2013**, 25, 4966−4985.

(10) Abel, P. R.; Chockla, A. M.; Lin, Y. M.; Holmberg, V. C.; Harris, J. T.; Korgel, B. A.; Heller, A.; Mullins, C. B. Buddie Mullins. Nanostructured Si(1-x)Gex for Tunable Thin Film Lithium-Ion Battery Anodes. *ACS Nano* **2013**, 7, 2249−2257.

(11) Zhai, T.; Xie, S. L.; Yu, M. H.; Fang, P. P.; Liang, C. L.; Lu, X. H.; Tong, Y. X. Oxygen Vacancies Enhancing Capacitive Properties of MnO$_2$ Nanorods for Wearable Asymmetric Supercapacitors. *Nano Energy* **2014**, 8, 255−263.

(12) Jin, S. X.; Wang, C. X. Synthesis and First Investigation of Excellent Lithium Storage Performances of Fe$_2$GeO$_4$/Reduced Graphene Oxide Nanocomposite. *Nano Energy* **2014**, *7*, 63−71.

(13) Yang, G. Z.; Song, H. W.; Cui, H.; Liu, Y. C.; Wang, C. X. Ultrafast Li-ion Battery Anode with Superlong Life and Excellent Cycling Stability from Strongly Coupled ZnO Nanoparticle/ Conductive Nanocarbon Skeleton Hybrid Materials. *Nano Energy* **2013**, *2*, 579−585.

(14) Wang, H. B.; Pan, Q. M.; Cheng, Y. X.; Zhao, J. W.; Yin, G. P. Evaluation of ZnO Nanorod Arrays with Dandelion-like Morphology as Negative Electrodes for Lithium-ion Batteries. *Electrochim. Acta* **2009**, *54*, 2851−2855.

(15) Li, C.; Yu, Z. S.; Fang, S. M.; Wang, H. X.; Gui, Y. H.; Xu, J. Q.; Chen, R. F. Preparation and Performance of ZnO Nanoparticle Aggregation with Porous Morphology. *J. Alloys Compd.* **2009**, *475*, 718−722.

(16) Kushima, A.; Liu, X. H.; Zhu, G.; Wang, Z. L.; Huang, J. Y.; Li, J. Leapfrog Cracking and Nanoamorphization of ZnO Nanowires during In Situ Electrochemical Lithiation. *Nano Lett.* **2011**, *11*, 4535−4541.

(17) Su, Q. M.; Dong, Z. M.; Zhang, J.; Du, G. H.; Xu, B. S. Visualizing the Electrochemical Reaction of ZnO Nanoparticles with Lithium by *in situ* TEM: Two Reaction Modes are Revealed. *Nanotechnology* **2013**, *24*, 255705.

(18) Liu, J. P.; Li, Y. Y.; Ding, R. M.; Jiang, J.; Hu, Y. Y.; Ji, X. X.; Chi, Q. B.; Zhu, Z. H.; Huang, X. T. Carbon/ZnO Nanorod Array Electrode with Significantly Improved Lithium Storage Capability. *J. Phys. Chem. C* **2009**, *113*, 5336−5339.

(19) Belliard, F.; Connor, P. A.; Irvine, J. T. S. Novel Tin Oxide-based Anodes for Li-ion Batteries. *Solid State Ionics* **2000**, *135*, 163−167.

(20) Paek, S. M.; Yoo, E.; Honma, I. Enhanced Cyclic Performance and Lithium Storage Capacity of SnO$_2$/Graphene Nanoporous Electrodes with Three-Dimensionally Delaminated Flexible Structure. *Nano Lett.* **2009**, *9*, 72−75.

(21) Kim, H.; Kim, S. W.; Park, Y. U.; Gwon, H.; Seo, D. H.; Kim, Y. SnO$_2$/Graphene Composite with High Lithium Storage Capability for Lithium Rechargeable Batteries. *Nano Res.* **2010**, *3*, 813−821.

(22) Wang, Y.; Zeng, H. C.; Lee, J. Y. Highly Reversible Lithium Storage in Porous SnO$_2$ Nanotubes with Coaxially Grown Carbon Nanotube Overlayers. *Adv. Mater.* **2006**, *18*, 645−649.

(23) Derrien, G.; Hassoun, J.; Panero, S.; Scrosati, B. Nanostructured Sn-C Composite as an Advanced Anode Material in High-performance Lithium-ion Batteries. *Adv. Mater.* **2007**, *19*, 2336−2340.

(24) Ko, S.; Lee, J. I.; Yang, H. S.; Park, S. S.; Jeong, U. Mesoporous CuO Particles Threaded with CNTs for High-Performance Lithium-Ion Battery Anodes. *Adv. Mater.* **2012**, *24*, 4451−4456.

(25) Song, H. W.; Li, N.; Cui, H.; Wang, C. X. Enhanced Storage Capability and Kinetic Processes by Pores- and Hetero-atoms- riched Carbon Nanobubbles for Lithium-ion and Sodium-ion batteries anodes. *Nano Energy* **2014**, *4*, 81−87.

(26) Sun, Y.; Chen, Y. Z.; Ding, C. R.; Yang, G. W.; Ma, Y. M.; Wang, C. X. One-Dimensional Al$_4$O$_4$C Ceramics: A New Type of Blue Light Emitter. *Sci. Rep.* **2013**, *3*, 1749.

(27) Sun, Y.; Cui, H.; Pang, C. L.; Wang, C. X. Structural Investigation of Epitaxial 2H-SiC-alpha-Al$_2$O$_3$ 1-D Heterostructures. *CrystEngComm* **2013**, *15*, 6477−6482.

(28) Sun, Y.; Jin, S. X.; Cui, H.; Wang, C. X. Eutectic Solidification Applied to Nanofabrication: A Strategy to Prepare Large-scale Tungsten Carbide Nanowalls. *J. Mater. Chem.* **2012**, *22*, 16566−16571.

(29) Kibel, M. H.; Leech, P. W. X-ray Photoelectron Spectroscopy Study of Optical Waveguide Glasses. *Surf. Interface Anal.* **1996**, *24*, 605−610.

(30) Hollinger, G.; Kumurdjian, P.; Mackowski, J. M.; Pertosa, P.; Porte, L.; Duc, T. M. ESCA Study of Molecular GeS$_{3-x}$Te xAs$_2$ Glasses. *J. Electron Spectrosc. Relat. Phenom.* **1974**, *5*, 237−245.

(31) Qiu, Y. F.; Fan, H. B.; Tan, G. P.; Yang, M. L.; Yang, X. X.; Yang, S. H. Effect of Nitrogen Doping on the Photo-catalytic Properties of Nitrogen Doped ZnO Tetrapods. *Mater. Lett.* **2014**, *131*, 64−66.

(32) Husain, S.; Alkhtaby, L. A.; bhat, I.; Giorgetti, E.; Zoppi, A.; Muniz Miranda, M. Study of Cobalt Doping on Structural and Luminescence Properties of Nanocrystalline ZnO. *J. Lumin.* **2014**, *154*, 430−436.

(33) Kaewmaraya, T.; De Sarkar, A.; Sa, B. S.; Sun, Z.; Ahuja, R. Strain-induced Tunability of Optical and Photocatalytic Properties of ZnO Mono-layer Nanosheet. *Comput. Mater. Sci.* **2014**, *91*, 38−42.

(34) Li, W. L.; Sheng, P. T.; Feng, H. Y.; Yin, X. H.; Zhu, X. W.; Yang, X.; Cai, Q. Y. Stable Core/Shell CdTe/Mn-CdS Quantum Dots Sensitized Three-Dimensional, Macroporous ZnO Nanosheet Photoelectrode and Their Photoelectrochemical Properties. *ACS Appl. Mater. Interfaces* **2014**, *6*, 12353−12362.

(35) Yu, Y. L.; Zhang, P.; Guo, L. M.; Chen, Z. D.; Wu, Q.; Ding, Y. H.; Zheng, W. J.; Cao, Y. The Design of TiO2 Nanostructures (Nanoparticle, Nanotube, and Nanosheet) and Their Photocatalytic Activity. *J. Phys. Chem. C* **2014**, *118*, 12727−12733.

(36) Yu, S. H.; CÖlfen, H.; Antonietti, M. Polymer-Controlled Morphosynthesis and Mineralization of Metal Carbonate Super-structures. *J. Phys. Chem. B* **2003**, *107*, 7396−7405.

(37) Yu, S. H.; Antonietti, M.; CÖlfen, H.; Hartmann, J. Growth and Self-Assembly of BaCrO4 and BaSO4 Nanofibers toward Hierarchical and Repetitive Superstructures by Polymer-Controlled Mineralization Reactions. *Nano Lett.* **2003**, *3*, 379−382.

(38) Yu, S. H.; CÖlfen, H.; Antonietti, M. Control of the Morphogenesis of Barium Chromate by Using Double Hydrophilic Block Copolymers (DHBCs) as Crystal Growth Modifiers. *Chem. - Eur. J.* **2002**, *8*, 2937−2946.

(39) Jia, F. F.; Song, L. X.; Wei, W.; Qu, P.; Xu, M. T. Facile one-pot method synthesis CNT−GeO$_2$ nanocomposite for high performance Li ion battery anode material. *New J. Chem.* **2015**, *39*, 689−695.

(40) Qiu, H. Y.; Zeng, L. X.; Lan, T. B.; Ding, X. K.; Wei, M. D. In situ synthesis of GeO$_2$/reduced graphene oxide composite on Ni foam substrate as a binder-free anode for high-capacity lithium-ion batteries. *J. Mater. Chem. A* **2015**, *3*, 1619.

(41) Seng, K. H.; Park, M.; Guo, Z. P.; Liu, H. K.; Cho, J. Catalytic Role of Ge in Highly Reversible GeO$_2$/Ge/C Nanocomposite Anode Material for Lithium Batteries. *Nano Lett.* **2013**, *13*, 1230−1236.

(42) Ahmad, M.; Shi, Y. Y.; Nisar, A.; Sun, H. Y.; Shen, W. C.; Miao, W. E.; Zhu, J. Synthesis of Hierarchical Flower-like ZnO Nanostructures and Ttheir Functionalization by Au Nanoparticles for Improved Photocatalytic and High Performance Li-ion Battery Anodes. *J. Mater. Chem.* **2011**, *21*, 7723.

(43) Huang, X. H.; Xia, X. H.; Yuan, Y. F.; Zhou, F. Porous ZnO Nanosheets Grown on Copper Substrates as Anodes for Lithium Ion Batteries. *Electrochim. Acta* **2011**, *56*, 4960−4965.

(44) Bresser, D.; Mueller, F.; Fiedler, M.; Krueger, S.; Kloepsch, R.; Baither, D.; Winter, M.; Paillard, E.; Passerini, S. Transition-Metal-Doped Zinc Oxide Nanoparticles as a New Lithium-Ion Anode Material. *Chem. Mater.* **2013**, *25*, 4977−4985.